Flat galaxy rotation curves from a Bennett-pinch plasma current: a two-parameter test on 175 SPARC galaxies

Kirk Bagger
Independent researcher

November 2026

Abstract

We test a quantitative plasma-current model of disk-galaxy rotation against the 175 rotation curves (3,391 measured points) of the SPARC database (Spitzer Photometry and Accurate Rotation Curves). In the model, an axial electric current I with a Bennett-pinch radial profile of core radius r_c produces an azimuthal magnetic field $B_\phi(r) = \mu_0 I r/[2\pi(r^2 + r_c^2)]$. The $\mathbf{J} \times \mathbf{B}$ force on current-carrying matter adds an acceleration proportional to B_ϕ to the Newtonian acceleration of the observed stars and gas. Far from the core this term falls as $1/r$ and adds a constant to V^2. With stellar mass-to-light ratios fixed at 0.5 (disk) and 0.7 (bulge) at 3.6 μm, we fit two parameters per galaxy (an amplitude K and r_c) by least squares. We compare the fits with Newtonian baryons alone (0 free parameters), a pure $1/r$ filament term (1 parameter), the radial acceleration relation (RAR) fitting function used in MOND-style analyses (0 and 2 parameters), and two-parameter Burkert and NFW dark-matter halos. All models are fitted with the same data, uncertainties, mass-to-light treatment, optimizer and degrees-of-freedom counting. Median reduced χ^2 values are 85.2 (Newtonian baryons), 11.7 ($1/r$ filament), 0.71 (Bennett pinch), 10.5 (RAR, fixed a_0), 1.35 (RAR, fitted a_0 and disk mass-to-light ratio), 0.71 (Burkert halo) and 1.28 (NFW halo). The fractions of galaxies with reduced $\chi^2 < 2$ are 3%, 11%, 73%, 11%, 64%, 70% and 59%, respectively. Among the four two-parameter models, the Bennett-pinch fit has the lowest χ^2 in head-to-head comparisons with the Burkert halo in 117 of 175 galaxies, with the NFW halo in 135, and with the two-parameter RAR in 128, and the lowest summed χ^2 over the sample. We convert K to a current under the stated assumption that the rotating matter carries the current uniformly per unit mass over a 1 kpc path. This gives a median $I = 4.3 \times 10^{18}$ A (16th–84th percentile 8.6×10^{17}–2.9×10^{19} A). For 83% of galaxies, I exceeds the $\sim 10^{18}$ A derived from Faraday rotation in the kpc-scale jet of 3C 303. The implied field at 10 kpc has a median of 15 μG (16th–84th percentile 4–100 μG). For 53% of galaxies it falls within the 3–30 μG range reported for spiral galaxies, and for 36% it exceeds 30 μG. The fitted velocity scale $\sqrt{K}$ correlates with the measured flat rotation velocity (Spearman $\rho = 0.94$). We list as quantities what the model requires: current magnitudes, field strengths, and coupling of the electromagnetic force to neutral gas and stars. K and r_c are fitted per galaxy and are not predicted from other galaxy properties. The model predicts a definite field strength, radial field profile, and field sign pattern for every galaxy, which radio polarization and Faraday-rotation surveys (LOFAR, SKA) can test independently of rotation curves.

1 Introduction

The open problem and the result in brief. In disk galaxies, the measured orbital speeds of gas and stars at large radii exceed what Newtonian gravity gives for the stars and gas that are observed. The usual way to close this gap adds unseen dark matter, but no laboratory direct-detection experiment has yet recorded a confirmed dark-matter particle signal. Another way modifies the

law of gravity at low accelerations (MOND). This paper tests a third option, stated quantitatively: an electric current flowing along each galaxy's rotation axis, whose magnetic field exerts a $\mathbf{J} \times \mathbf{B}$ force on the rotating matter. With a Bennett-pinch current profile and two free parameters per galaxy, the model fits the 175 SPARC rotation curves with a median reduced χ^2 of 0.71. 73% of galaxies have reduced $\chi^2 < 2$. Fitted by the same procedure and with the same number of free parameters, a Burkert dark-matter halo gives a median of 0.71 and 70% below 2, an NFW halo 1.28 and 59%, and a two-parameter MOND-style (RAR) fit 1.35 and 64%. The Bennett-pinch fit has the lower χ^2 in 117 of 175 galaxies against the Burkert halo, 135 against NFW and 128 against the RAR fit. The same fits also give each galaxy a definite current in amperes and a field in microgauss. Those numbers can be checked against radio measurements, and some of them sit above the values measured so far (Sections 5.3–6).

Rotation curves. A rotation curve is the circular speed $V(r)$ of gas or stars in a disk galaxy as a function of distance r from the galaxy centre. It is measured from Doppler shifts of the 21 cm line of neutral hydrogen (H I) and of optical emission lines such as Hα. Optical and H I rotation curves of spiral galaxies remain approximately flat to the largest measured radii (Rubin et al., 1980; Bosma, 1981; Sofue and Rubin, 2001). In Newtonian gravity, the circular speed produced by the observed stars and gas alone (the "baryons") falls with radius beyond the bulk of the light. The measured speeds exceed it at large radii. This difference between the measured $V(r)$ and the Newtonian baryonic curve $V_{\rm bar}(r)$ is the observation addressed here.

Magnetic fields in and between galaxies. Galactic magnetic fields are measured mainly through two effects. One is synchrotron radio emission from relativistic electrons spiralling in the field. The other is Faraday rotation: the rotation of the polarization angle of linearly polarized radio waves as they pass through a magnetized plasma, by an angle proportional to the square of the wavelength times the rotation measure $\mathrm{RM} \propto \int n_e B_\parallel \, dl$, where n_e is the free-electron density and $B_\parallel$ the field component along the line of sight. Beck (2015) reports equipartition total field strengths, corrected for inclination, of $9 \pm 2\,\mu$G averaged over 74 spiral galaxies and $17 \pm 3\,\mu$G averaged over 21 bright galaxies. The same review gives 20–30 μG in the spiral arms of gas-rich, star-forming spirals, 50–100 μG in starburst regions, and about 6 μG in radio-faint galaxies such as M 31 and M 33. Milky Way field measurements and models are reviewed by Han (2017), and a model of the Galactic field fitted to Faraday rotation and synchrotron data is given by Jansson and Farrar (2012). On larger scales, LOFAR observations at 140 MHz show a radio ridge about 3 Mpc long between the galaxy clusters Abell 399 and Abell 401, which requires magnetic fields and relativistic electrons along the filament (Govoni et al., 2019).

Measured currents. From radio, polarization and Faraday-rotation maps of the 50 kpc jet of the radio galaxy 3C 303, Kronberg et al. (2011) derived a galactic-scale axial electric current of $\sim 10^{18}$ A, directed away from the active nucleus. We use this value as the reference current magnitude below.

Plasma filaments and pinches. A Birkeland current, named for the field-aligned currents studied by Birkeland (1908), is a current that flows along magnetic field lines in a plasma. Two parallel currents attract through their magnetic fields, and a current column is compressed by its own azimuthal field. Bennett (1934) derived the equilibrium of such a self-focussing current stream. In that equilibrium, now called the Bennett pinch, the magnetic pressure of the current's own field balances the thermal pressure of the plasma. The resulting current-density profile has a finite core and falls off as a power law outside it. Alfvén (1981) and Alfvén (1986) described cosmic plasmas in

terms of currents, circuits and double layers. Peratt and Green (1983) and Peratt (1986a,b) carried out particle-in-cell simulations of interacting, current-carrying galactic-scale plasma filaments. In those simulations the interaction force between filaments varies as $1/r$ and produces flat rotation profiles.

Related work. The idea that magnetic or current-related forces can contribute to disk rotation predates this paper, and this paper does not claim priority for it. Nelson (1988) showed, in a cylindrical model, that magnetic stress in the outer gaseous disk can raise rotation speeds above the gravitational speed of the visible matter. Battaner et al. (1992) developed an azimuthal-field alternative to dark matter and applied it to M31. Battaner and Florido (1995) constructed a two-dimensional magnetohydrodynamic model of that process. Ruiz-Granados et al. (2010) and Ruiz-Granados et al. (2012) fitted a magnetic contribution, together with luminous mass and a dark halo, to the outer rotation curves of M31 and the Milky Way. Tsiklauri (2011) fitted a $\mathbf{J} \times \mathbf{B}$ term, using a more realistic Galactic field model, to the Milky Way rotation curve. Holmes (2026) applied a magnetohydrodynamic boundary-stress analysis to all 175 SPARC galaxies and reported a relation between a plasma-instability parameter and the residuals between observed and baryonic speeds. The present paper differs from those works in the model and the test: it fits a two-parameter Bennett-pinch current profile to every SPARC rotation curve, converts the amplitudes into currents and field strengths, and compares the fits with Burkert, NFW and RAR models under one and the same procedure.

This work. We write down a specific, parameterized version of a current-driven rotation model. We fit it to every galaxy in a public database with measured baryon decompositions, and we report the fit statistics and the physical quantities (current in amperes, field in microgauss) that the fits require. For reference we also fit five other curves to the same data with the same procedure: (i) Newtonian baryons alone; (ii) a pure $1/r$ filament term; (iii) the radial acceleration relation (RAR) fitting function; and (iv, v) the Burkert and NFW dark-matter halo profiles. MOND (Modified Newtonian Dynamics; Milgrom 1983) is a proposal in which the acceleration departs from the Newtonian value below a characteristic scale $a_0 \approx 10^{-10}\,\mathrm{m\,s^{-2}}$. The RAR is an empirical relation between the observed centripetal acceleration and the Newtonian baryonic acceleration measured in SPARC galaxies (McGaugh et al., 2016; Lelli et al., 2017). Its fitting function has the same form as a commonly used MOND interpolation function. We report numbers only and do not rank the models beyond the statistics given.

Prior work used here. The physical and observational ingredients of this paper are the work of others. They are the field-aligned currents of Birkeland (1908); the Bennett-pinch equilibrium (Bennett, 1934); the description of cosmic plasmas in terms of currents and circuits (Alfvén, 1981, 1986); the simulations of interacting galactic plasma filaments and the $1/r$ filament force (Peratt and Green, 1983; Peratt, 1986a,b); the demonstration that magnetic stress can raise outer-disk rotation (Nelson, 1988); the azimuthal-field model and its two-dimensional magnetohydrodynamic development (Battaner et al., 1992; Battaner and Florido, 1995); later magnetic and $\mathbf{J} \times \mathbf{B}$ fits to M31 and the Milky Way (Ruiz-Granados et al., 2010, 2012; Tsiklauri, 2011); an MHD residual analysis of the SPARC sample (Holmes, 2026); the SPARC rotation curves and mass models (Lelli et al., 2016); MOND (Milgrom, 1983) and the RAR fitting function (McGaugh et al., 2016); the Burkert profile (Burkert, 1995), the NFW profile (Navarro et al., 1996) and the published halo fits to SPARC (Li et al., 2020); the measured field strengths (Beck, 2015; Han, 2017); the LOFAR radio ridge (Govoni et al., 2019); and the jet current derived from Faraday rotation (Kronberg et al.,

2011). This paper claims no priority for any of these ideas or data.

Contributions of this work. This paper's contribution is a uniform test of one parameterized model, not a claim to have originated the idea that currents or magnetic fields can affect rotation. The work consists of the following items, each of which can be checked against the code and tables released with this paper.

C1. A per-galaxy fit of a Bennett-pinch axial-current model with a fitted core radius (Eq. 4) to all 175 SPARC rotation curves (3,391 points), with fixed stellar mass-to-light ratios.

C2. Scoring of that model on the same data, errors, mass-to-light treatment, optimizer and χ^2 definition as six reference curves: Newtonian baryons, a pure $1/r$ filament term, the RAR function with fixed and fitted a_0, and two-parameter Burkert and NFW dark-matter halos. All two-parameter models are compared galaxy by galaxy. The published halo fits of Li et al. (2020) serve as an independent cross-check.

C3. Conversion of each fitted amplitude into a current in amperes, under an explicitly stated path-length assumption, with its scaling given ($I \propto L^{-1/2} M_b^{1/2}$). The resulting distribution is compared with the $\sim 10^{18}$ A derived from Faraday rotation in the 3C 303 jet.

C4. Calculation of the implied azimuthal field at 10 kpc for each galaxy and comparison with the field strengths reported for spiral galaxies.

C5. The inverse calculation: the current-length per kilogram ($\approx 0.05\,\mathrm{A\,m\,kg^{-1}}$) and the co-rotating charge imbalance ($\approx$ 5 unbalanced charges per 10^{15} protons) that the fitted accelerations require if the field is fixed at 5 μG.

C6. Correlations of the fitted current and velocity scale with measured galaxy properties, a list of the model's requirements stated as quantities (Section 6), and per-galaxy predictions that observations can check (Section 7).

C7. Public release of the analysis code and per-galaxy results (Appendix A and `anc/`).

Why this matters. A model that only matches rotation curves cannot be told apart from other models that match them equally well. This one also commits to physical quantities that can be measured independently of rotation: the current, the field strength, and the field's radial shape for each galaxy. In this sample the fit quality is comparable to that of the two-parameter models already in use (Table 1). The model's required fields fall inside the measured spiral-galaxy range for about half the galaxies and above it for about a third (Section 5.4). That makes the test sharp. Radio polarization and Faraday-rotation surveys can confirm or rule out the predicted fields galaxy by galaxy, without reference to rotation curves.

2 Data

SPARC (Lelli et al., 2016) is a database of 175 disk galaxies with Spitzer 3.6 μm photometry and H I/Hα rotation curves compiled from the literature. For each galaxy it provides, at each measured radius r_i:

- $V_{\rm obs}(r_i)$ and its uncertainty σ_i ($\mathrm{km\,s^{-1}}$): the measured rotation speed and its error;
- $V_{\rm gas}(r_i)$ ($\mathrm{km\,s^{-1}}$): the Newtonian circular speed of the H I gas disk alone, computed from the measured H I surface density (scaled by 1.33 for helium);
- $V_{\rm disk}(r_i)$ and $V_{\rm bul}(r_i)$ ($\mathrm{km\,s^{-1}}$): the Newtonian circular speeds of the stellar disk and bulge alone, computed from the 3.6 μm surface brightness for a mass-to-light ratio of 1 $M_\odot/L_\odot$.

The galaxy table supplies the distance, inclination, total 3.6 μm luminosity $L_{[3.6]}$, disk scale length R_d, disk central surface brightness, total H I mass $M_{\rm HI}$, flat rotation velocity $V_{\rm flat}$ (where de-

fined), Hubble type T, and a quality flag Q (1 = high, 2 = medium, 3 = low). We used the files `Rotmod_LTG.zip` (175 mass-model files) and `SPARC_Lelli2016c.mrt`, downloaded from https://astroweb.cwru.edu/SPARC/ on 2026 November 18. The sample contains 3,391 rotation-curve points, with a median of 14 points per galaxy; 99 galaxies have $Q = 1$, 64 have $Q = 2$ and 12 have $Q = 3$. No galaxy was excluded.

3 Models

All velocities are in $\mathrm{km\,s^{-1}}$, radii in kpc, accelerations in $\mathrm{m\,s^{-2}}$, magnetic fields in tesla (T) or microgauss ($1\,\mu\mathrm{G} = 10^{-10}\,\mathrm{T}$), and currents in amperes (A). $\mu_0 = 4\pi \times 10^{-7}\,\mathrm{T\,m\,A^{-1}}$ is the vacuum permeability, $1\,\mathrm{kpc} = 3.0857 \times 10^{19}\,\mathrm{m}$ and $1\,M_\odot = 1.989 \times 10^{30}\,\mathrm{kg}$.

3.1 Model N: Newtonian baryons

$$V_{\rm bar}^2(r) = V_{\rm gas}|V_{\rm gas}| + \Upsilon_d\, V_{\rm disk}|V_{\rm disk}| + \Upsilon_b\, V_{\rm bul}|V_{\rm bul}|. \tag{1}$$

Here $V_{\rm bar}$ is the circular speed produced by the observed gas and stars under Newtonian gravity. Υ_d and Υ_b are the stellar mass-to-light ratios of the disk and bulge at 3.6 μm (solar units, $M_\odot/L_\odot$), fixed at $\Upsilon_d = 0.5$ and $\Upsilon_b = 0.7$ (Lelli et al., 2016; Schombert and McGaugh, 2014). The form $V|V|$ keeps the sign of each component: SPARC lists a negative $V_{\rm gas}$ where the gas distribution produces a net outward pull, as in central H I holes. The model speed is $V_N = \sqrt{\max(V_{\rm bar}^2, 0)}$. Model N has no free parameters.

3.2 Model E2: Bennett-pinch current

Field. We assume an axial current I (A) flowing parallel to the galaxy's rotation axis, with the Bennett-pinch current-density profile $J_z(r) = (I/\pi r_c^2)\,(1 + r^2/r_c^2)^{-2}$ (Bennett, 1934). J_z ($\mathrm{A\,m^{-2}}$) is the current density along the axis at cylindrical radius r, and r_c (kpc) is the core radius inside which the current is spread out. The current enclosed within radius r is $I(<r) = I\,r^2/(r^2 + r_c^2)$, and Ampère's law gives the azimuthal field

$$B_\phi(r) = \frac{\mu_0\, I(<r)}{2\pi r} = \frac{\mu_0 I}{2\pi}\,\frac{r}{r^2 + r_c^2}. \tag{2}$$

B_ϕ (T) is the field circling the axis at radius r. Far outside the core ($r \gg r_c$), $B_\phi \to \mu_0 I/(2\pi r)$, the field of a line current. Near the centre ($r \ll r_c$), B_ϕ rises linearly with r.

Force. Matter at radius r that carries axial current feels a radial Lorentz force $\mathbf{J} \times \mathbf{B}$, directed inward for current parallel to I. We write the resulting acceleration per unit mass as

$$a_{\rm EM}(r) = \eta\, B_\phi(r), \tag{3}$$

where η ($\mathrm{A\,m\,kg^{-1}}$) is the current-length carried per kilogram of rotating matter. For a wire element carrying current i over length ℓ with mass m, $\eta = i\ell/m$, and the force on it is $i\ell B$.

Rotation speed. For circular orbits the centripetal acceleration equals the total inward acceleration, $V^2/r = a_{\rm grav} + a_{\rm EM}$. With $a_{\rm grav} = V_{\rm bar}^2/r$:

$$V_{\rm E2}^2(r) = V_{\rm bar}^2(r) + K\,\frac{r^2}{r^2 + r_c^2}, \qquad K = \frac{\mu_0\, I\, \eta}{2\pi}. \tag{4}$$

K ($\mathrm{km^2\,s^{-2}}$) is the amplitude of the electromagnetic term, and $\sqrt{K}$ ($\mathrm{km\,s^{-1}}$) is the constant extra speed it adds in quadrature at $r \gg r_c$. Model E2 has two free parameters per galaxy, K and r_c. The fit constrains only the product $I\eta$, so converting K to amperes requires an additional assumption (Section 5.3).

3.3 Model E1: pure $1/r$ filament

Setting $r_c = 0$ in Eq. (4) gives the line-current case, in which $a_{\rm EM} \propto 1/r$ at all radii, as in the filament interaction of Peratt (1986b):

$$V_{\rm E1}^2(r) = V_{\rm bar}^2(r) + K. \tag{5}$$

Model E1 has one free parameter, K ($\mathrm{km^2\,s^{-2}}$).

3.4 Models R0 and R2: radial acceleration relation (MOND-style reference)

With $g_{\rm bar} = V_{\rm bar}^2/r$ the Newtonian baryonic acceleration ($\mathrm{m\,s^{-2}}$), the RAR fitting function (McGaugh et al., 2016) gives the predicted acceleration

$$g_{\rm RAR} = \frac{g_{\rm bar}}{1 - \exp\!\left(-\sqrt{g_{\rm bar}/a_0}\right)}, \qquad V_{\rm RAR} = \sqrt{g_{\rm RAR}\, r}. \tag{6}$$

a_0 ($\mathrm{m\,s^{-2}}$) is the acceleration scale below which $g_{\rm RAR}$ departs from $g_{\rm bar}$. Model R0 fixes $a_0 = 1.2 \times 10^{-10}\,\mathrm{m\,s^{-2}}$ and $\Upsilon_d = 0.5$ (0 free parameters). Model R2 fits a_0 and Υ_d per galaxy (2 free parameters), giving it the same number of free parameters as E2. Points with $V_{\rm bar}^2 \le 0$ are assigned $V_{\rm RAR} = 0$.

3.5 Models BUR and NFW: dark-matter halos

In both halo models the halo's circular speed is added in quadrature to the fixed-Υ baryonic curve, $V^2 = V_{\rm bar}^2 + V_{\rm halo}^2$, exactly as the electromagnetic term is added in E2. $G = 4.30091 \times 10^{-6}\,\mathrm{kpc\,(km\,s^{-1})^2\,}M_\odot^{-1}$ is the gravitational constant.

Burkert (BUR). The Burkert profile is a cored density profile (Burkert, 1995), $\rho(r) = \rho_0 r_0^3/[(r + r_0)(r^2 + r_0^2)]$, with central density ρ_0 ($M_\odot\,\mathrm{kpc^{-3}}$) and core radius r_0 (kpc). Its enclosed mass gives

$$V_{\rm BUR}^2(r) = \frac{G}{r}\,\pi\rho_0 r_0^3 \left[\ln\!\left((1+x)^2(1+x^2)\right) - 2\arctan x\right], \qquad x = r/r_0. \tag{7}$$

Free parameters: $\log_{10}\rho_0$ and r_0 ($k = 2$).

NFW. The Navarro–Frenk–White profile (Navarro et al., 1996), $\rho(r) \propto [(r/r_s)(1 + r/r_s)^2]^{-1}$, is the cuspy profile found in cold-dark-matter simulations. In terms of the circular speed V_{200} at the radius R_{200}, within which the mean density is 200 times the critical density, and the concentration $c = R_{200}/r_s$,

$$V_{\rm NFW}^2(r) = V_{200}^2\,\frac{f(cx)}{x\,f(c)}, \qquad f(y) = \ln(1+y) - \frac{y}{1+y}, \qquad x = r/R_{200}, \tag{8}$$

with $R_{200} = V_{200}/(10H_0)$ and $H_0 = 73\,\mathrm{km\,s^{-1}\,Mpc^{-1}}$. Free parameters: V_{200} and c ($k = 2$). No concentration–mass relation is imposed.

3.6 Assumptions

A1. **Baryon decomposition.** The SPARC $V_{\rm gas}$, $V_{\rm disk}$, $V_{\rm bul}$ are used as given, including the 1.33 helium factor in $V_{\rm gas}$ and the SPARC distances and inclinations.

A2. **Mass-to-light ratios.** $\Upsilon_d = 0.5$, $\Upsilon_b = 0.7$ ($M_\odot/L_\odot$ at 3.6 μm), fixed in N, E1, E2, R0, BUR and NFW; $\Upsilon_b = 0.7$ fixed and Υ_d free in R2. A supplementary run with Υ_d also free in E2, BUR and NFW is reported in Section 5.2.

A3. **Current geometry.** A single axial current with a Bennett-pinch radial profile (Eq. 2), symmetric about the rotation axis and steady in time. No return current is included inside the fitted radii.

A4. **Force law.** The electromagnetic acceleration is radial and inward, $a_{\rm EM} = \eta B_\phi$, with η independent of radius.

A5. **Coupling to all rotating matter.** The measured rotation speeds come from H I (mostly neutral) and Hα gas, and stars move with them. The model therefore assumes that the force acting on the ionized, current-carrying component is transferred to neutral gas and stars, for example by collisions. This transfer is assumed and is not tested here.

A6. **Circular orbits.** The measured speeds are circular speeds; pressure support and non-circular motions are neglected.

A7. **Current carried by the rotating matter (amps conversion only).** The axial current is carried by the rotating baryons uniformly per unit mass over a path length $L = 1\,$kpc through the disk (Section 5.3).

A8. **Baryonic mass (amps conversion only).** $M_b = 0.5\,L_{[3.6]} + 1.33\,M_{\rm HI}$ (in $M_\odot$, with $L_{[3.6]}$ in $L_\odot$). The bulge is included in $L_{[3.6]}$ at $\Upsilon = 0.5$. A gas-only variant uses $M_g = 1.33\,M_{\rm HI}$.

A9. **Uncertainties.** Only the SPARC velocity uncertainties are used, with a floor of $1\,{\rm km\,s^{-1}}$. Distance and inclination uncertainties are not propagated.

4 Fitting method

For each galaxy and model we minimize

$$\chi^2 = \sum_{i=1}^{N} \left[\frac{V_{\rm obs}(r_i) - V_{\rm model}(r_i)}{\sigma_i} \right]^2 , \tag{9}$$

where N is the number of rotation-curve points in the galaxy and $\sigma_i = \max(\sigma_{{\rm obs},i}, 1\,{\rm km\,s^{-1}})$ is the velocity uncertainty. The reduced chi-squared is $\chi^2_\nu = \chi^2/(N-k)$, where k is the number of free parameters (0 for N and R0, 1 for E1, 2 for E2, R2, BUR and NFW). $\chi^2_\nu \approx 1$ means the model deviates from the data by about the quoted uncertainties. $\chi^2_\nu \gg 1$ means the deviations are larger than the uncertainties. $\chi^2_\nu < 1$ means they are smaller than the uncertainties, which happens when uncertainties are overestimated, when points are correlated, or when the model has enough freedom to follow the noise. Every galaxy has $N \geq 4$, so $N - k \geq 2$ for all models.

Minimization uses the bounded trust-region least-squares solver `least_squares` from the `scipy.optimize` module (Virtanen et al., 2020), with NumPy (Harris et al., 2020) and Matplotlib (Hunter, 2007). The parameter bounds are listed below. No priors are applied, so each fit is a maximum-likelihood fit within its bounds.

- E1: $0 \le K \le 10^6\,\mathrm{km^2\,s^{-2}}$; starting value $\max[\mathrm{median}(V_{\rm obs}^2 - V_{\rm bar}^2), 1]$.
- E2: $0 \le K \le 10^6\,\mathrm{km^2\,s^{-2}}$ and $0.01 \le r_c \le 200\,\mathrm{kpc}$. The fit is run from six starting values of r_c (0.01, 0.1, 1, 3, 10, 30 kpc) with the E1 value of K, and the lowest χ^2 is kept.
- R2: $0.01 \le a_0/(10^{-10}\,\mathrm{m\,s^{-2}}) \le 20$, $0.05 \le \Upsilon_d \le 2.0$; start at (1.2, 0.5).
- BUR: $3 \le \log_{10}[\rho_0/(M_\odot\,\mathrm{kpc^{-3}})] \le 12$ and $0.01 \le r_0 \le 200\,\mathrm{kpc}$. Run from the same six starting values of r_0 as r_c in E2, each with ρ_0 chosen so that $V_{\rm BUR}^2$ at the outermost point equals the E1 value of K; the lowest χ^2 is kept.
- NFW: $1 \le V_{200} \le 1000\,\mathrm{km\,s^{-1}}$ and $1 \le c \le 100$. Run from six starting values of c (2, 4, 8, 15, 30, 60) with $V_{200} = \sqrt{K_{\rm E1}}$; the lowest χ^2 is kept.

As a check on the optimizer, every two-parameter model was refitted from a common grid of 30 starting points (the six scale starts above times five amplitude starts; for R2, 5 values of a_0 times 6 of Υ_d). No galaxy's E2, BUR or NFW χ^2 improved by more than 0.3%, and only one R2 fit improved by more than 1%; none of the statistics below changes at the quoted precision. The E2 and R2 fits reproduce those of the original analysis exactly. In four galaxies (NGC 5371, NGC 6674, PGC 51017, UGC 6628) the E2 fit reaches the lower bound $r_c = 0.01$ kpc and therefore reproduces E1. Its χ^2 is equal to the E1 value to within 3×10^{-3}, and its χ^2_ν is larger because E2 has one fewer degree of freedom.

For aggregate statistics we report the per-galaxy median χ^2_ν, the 16th and 84th percentiles, and the fraction of galaxies with $\chi^2_\nu < 1$, < 2 and < 5. We also report a pooled value, $\sum \chi^2 / \sum (N - k)$ over all galaxies. Correlations between fitted quantities and galaxy properties use the Spearman rank coefficient ρ, which measures how well the relation is described by a monotonic function ($\rho = \pm 1$ perfectly monotonic, $\rho = 0$ no monotonic trend), with its two-sided p-value.

5 Results

5.1 Fit statistics

Table 1: Fit statistics for the 175 SPARC galaxies (3,391 points). Columns: k = free parameters per galaxy; median and 16th–84th percentile range of per-galaxy χ^2_ν; fraction of galaxies below 1, 2 and 5; pooled $\chi^2_\nu = \sum \chi^2 / \sum (N - k)$. Compare rows with equal k: N vs. R0 ($k = 0$), and E2, R2, BUR and NFW ($k = 2$). All rows use the same data, uncertainties and fitting procedure.

Model	k	median χ^2_ν (16–84%)	< 1	< 2	< 5	pooled χ^2_ν
N: Newtonian baryons	0	85.2 (16.9–535)	2.3%	2.9%	6.3%	406
E1: $1/r$ filament	1	11.7 (2.9–49.7)	4.6%	11.4%	25.1%	36.6
E2: Bennett pinch	2	0.71 (0.14–4.39)	60.0%	73.1%	87.4%	4.46
R0: RAR, a_0 fixed	0	10.5 (2.5–53.6)	5.1%	11.4%	34.3%	39.1
R2: RAR, a_0, Υ_d fitted	2	1.35 (0.33–4.97)	41.1%	64.0%	84.0%	5.02
BUR: Burkert halo	2	0.71 (0.17–5.23)	57.7%	70.3%	83.4%	5.59
NFW: NFW halo	2	1.28 (0.34–5.73)	42.3%	58.9%	80.0%	5.83

Table 1 lists the fit statistics. For the two-parameter models, E2 gives a lower χ^2_ν than R2 in 128 of 175 galaxies (73%). A Wilcoxon signed-rank test on the paired per-galaxy χ^2_ν values gives $p = 7 \times 10^{-9}$. The Bayesian information criterion, $\mathrm{BIC} = \chi^2 + k \ln N$, summed over galaxies, is 1.45×10^4 for E2 and 1.62×10^4 for R2. E2 has a lower BIC than R2 in 73% of galaxies. The comparison with the dark-matter halo fits is given in Section 5.2. With only quality flags $Q = 1$–2 (163 galaxies), the median χ^2_ν is 0.71 (E2), 1.35 (R2), 12.0 (E1), 9.2 (R0) and 101 (N).

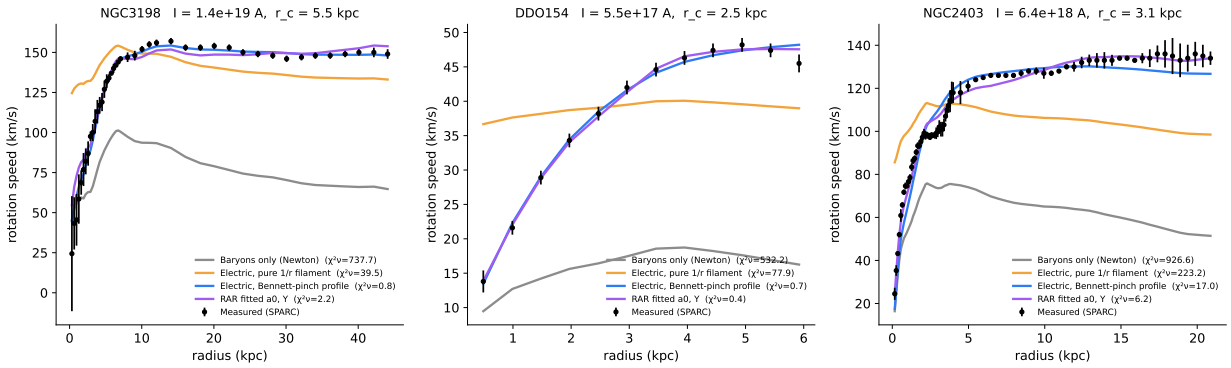


Figure 1: Rotation curves of NGC 3198, DDO 154 and NGC 2403. Black points: measured $V_{\rm obs}$ with uncertainties. Grey: Newtonian baryons (model N). Orange: $1/r$ filament (E1). Blue: Bennett pinch (E2). Purple: RAR with fitted a_0 and Υ_d (R2). The χ^2_ν of each model is given in the legend, and the fitted E2 current and core radius in each title. Compare the inner rising parts, where E1 departs from the data and E2 does not.

The fitted E2 parameters have median $\sqrt{K} = 100\,\mathrm{km\,s^{-1}}$ (16th–84th percentile 57–200 $\mathrm{km\,s^{-1}}$) and median $r_c = 3.4\,\mathrm{kpc}$ (1.4–10.1 kpc). Seven galaxies have $r_c > 50\,\mathrm{kpc}$, where the electromagnetic term rises over the whole measured range. The R2 fits have median $a_0 = 0.83 \times 10^{-10}\,\mathrm{m\,s^{-2}}$ (0.29–2.09) and median $\Upsilon_d = 0.53$ (0.10–1.41). Eight galaxies have E2 $\chi^2_\nu > 20$: UGC 6973 (83.5), NGC 4217 (33.7), UGC 2916 (33.0), IC 4202 (31.9), UGC 2455 (31.4), UGC 6787 (23.4), NGC 4389 (21.0) and UGC 3580 (20.5).

Table 2: Three example galaxies (Figure 1). N = number of points; χ^2_ν for each model; I = current from Eq. (10) (A); r_c (kpc); B_{10} = implied field at 10 kpc (μG).

Galaxy	N	N	E1	E2	R0	R2	I (A)	r_c	B_{10}
NGC 3198	43	738	39.5	0.77	13.3	2.25	1.4×10^{19}	5.5	70
DDO 154	12	532	77.9	0.71	16.0	0.40	5.5×10^{17}	2.5	3.4
NGC 2403	73	927	223	17.0	16.7	6.22	6.4×10^{18}	3.1	38

5.2 Comparison with dark-matter halo fits

The Burkert and NFW fits use the same data, the same σ_i, the same fixed Υ_d and Υ_b, the same optimizer with a six-point multi-start, and the same $\chi^2_\nu = \chi^2/(N-2)$ as E2 (Sections 3–4). All four two-parameter models therefore have equal k, and differences in summed χ^2, AIC ($\chi^2 + 2k$) and BIC are the same. Table 3 gives the galaxy-by-galaxy comparison and Figure 3 the distributions.

The Burkert halo and the Bennett pinch have nearly the same median χ^2_ν (0.710 and 0.706) and similar distributions (Figure 3). Galaxy by galaxy, E2 has the lower χ^2 in 117 of 175 cases, and its summed χ^2 is lower by 3.4×10^3. In 40 galaxies the NFW fit runs to the lower bound $c = 1$, which is the least cuspy shape the profile allows within these bounds. Refitting NFW with wider bounds ($0.1 \le c \le 1000$, $V_{200} \le 3000\,\mathrm{km\,s^{-1}}$) gives a median χ^2_ν of 1.26 and 59% below 2, with E2 still lower in 135 galaxies. The Burkert fit reaches a bound on r_0 in 7 galaxies.

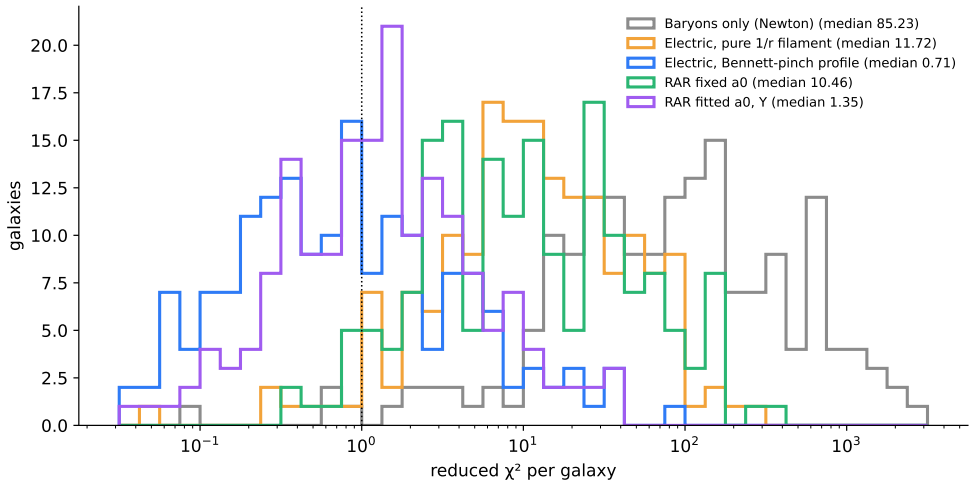


Figure 2: Distributions of per-galaxy χ^2_ν for the five models (logarithmic axis). The dotted line marks $\chi^2_\nu = 1$. Medians are given in the legend.

Table 3: Two-parameter models fitted by the same procedure to the 175 SPARC galaxies (3,391 points). "E2 lower" is the number of galaxies in which the Bennett-pinch fit has the lower χ^2; p is the two-sided Wilcoxon signed-rank test on the paired per-galaxy χ^2_ν. Summed AIC and BIC are $\sum(\chi^2 + 2k)$ and $\sum(\chi^2 + k \ln N)$.

Model ($k = 2$)	median χ^2_ν	< 1	< 2	E2 lower	p	$\sum$AIC / $\sum$BIC
E2: Bennett pinch	0.706	60.0%	73.1%	–	–	14,265 / 14,512
BUR: Burkert halo	0.710	57.7%	70.3%	117 / 175	6×10^{-6}	17,687 / 17,934
NFW: NFW halo	1.28	42.3%	58.9%	135 / 175	1×10^{-14}	18,423 / 18,670
R2: RAR, a_0, Υ_d	1.35	41.1%	64.0%	128 / 175	7×10^{-9}	15,975 / 16,222

Free stellar mass-to-light ratio. Because R2 fits Υ_d while E2, BUR and NFW use the fixed value, we also refitted E2, BUR and NFW with Υ_d free ($0.05 \le \Upsilon_d \le 2$, $k = 3$). The median χ^2_ν values become 0.45 (E2), 0.50 (BUR) and 0.99 (NFW), with 85%, 81% and 66% of galaxies below 2. Summed BIC is 1.05×10^4 (E2), 1.17×10^4 (BUR) and 1.37×10^4 (NFW), against 1.62×10^4 for R2 ($k = 2$) and 2.83×10^4 for an RAR fit with only a_0 free ($k = 1$). Per galaxy, the three-parameter E2 has a lower BIC than three-parameter BUR in 101 galaxies, than three-parameter NFW in 138, and than R2 in 123.

Cross-check with published fits. Li et al. (2020) fitted seven halo profiles to the same 175 SPARC galaxies with Markov-chain Monte Carlo, marginalizing over Υ_d, Υ_b, distance and inclination (with priors on each) as well as two halo parameters. From their machine-readable table (ApJS 247, 31, Table 1), the Burkert profile with flat priors has median $\chi^2_\nu = 0.97$ and $\chi^2_\nu < 2$ for 68.6% of galaxies, and NFW with flat priors 1.78 and 54.3% (ten galaxies without a finite listed χ^2_ν counted as ≥ 2). Their procedure differs from ours in priors, nuisance parameters and degrees-of-freedom counting, so the numbers are not expected to agree exactly. Both analyses find the cored Burkert profile fitting SPARC better than NFW and reaching $\chi^2_\nu < 2$ in about 70% of galaxies.

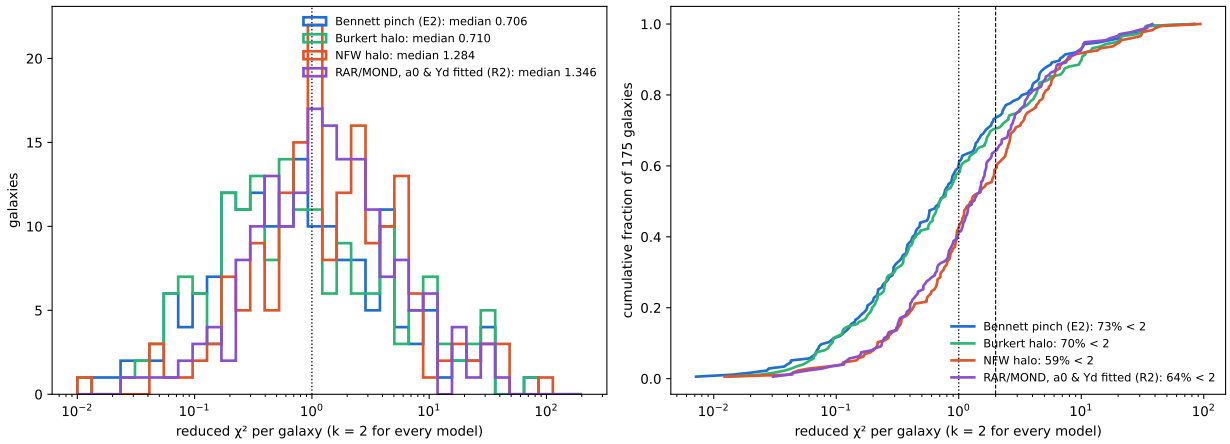


Figure 3: Per-galaxy χ^2_ν for the four two-parameter models, all fitted with the same data, uncertainties, fixed Υ (except Υ_d in R2) and optimizer. Left: histograms (logarithmic axis; medians in the legend). Right: cumulative distributions; the dashed line marks $\chi^2_\nu = 2$ and the legend gives the fraction of galaxies below it.

5.3 Fitted currents

Eq. (4) constrains only $K = \mu_0 I\eta/(2\pi)$. To express K in amperes we use assumptions A7 and A8, in the following steps.

1. Suppose the total axial current I is carried by the rotating baryons, distributed uniformly per kilogram, along a path of length L through the disk. A mass element dm then carries current $dI = I\,dm/M_b$ over length L, so the current-length per kilogram is $\eta = IL/M_b$.
2. Substituting into $K = \mu_0 I\eta/(2\pi)$ gives $K = \mu_0 I^2 L/(2\pi M_b)$.
3. Solving for I:
$$I = \sqrt{\frac{2\pi\, K\, M_b}{\mu_0\, L}}. \tag{10}$$
Here K is in $\mathrm{m^2\,s^{-2}}$ ($1\,\mathrm{km^2\,s^{-2}} = 10^6\,\mathrm{m^2\,s^{-2}}$), M_b in kg, L in m, and I in A.
4. We take $L = 1\,\mathrm{kpc}$. Because $I \propto L^{-1/2}$, $L = 0.1\,\mathrm{kpc}$ gives currents 3.16 times larger and $L = 10\,\mathrm{kpc}$ gives currents 3.16 times smaller. Because $I \propto M_b^{1/2}$, the gas-only variant (M_g instead of M_b) gives smaller currents.

Worked example (NGC 3198). The fit gives $K = 1.80 \times 10^4\,\mathrm{km^2\,s^{-2}} = 1.80 \times 10^{10}\,\mathrm{m^2\,s^{-2}}$ ($\sqrt{K} = 134\,\mathrm{km\,s^{-1}}$). The galaxy has $L_{[3.6]} = 3.83 \times 10^{10} L_\odot$ and $M_{\mathrm{HI}} = 1.09 \times 10^{10} M_\odot$, so $M_b = 0.5(3.83 \times 10^{10}) + 1.33(1.09 \times 10^{10}) = 3.36 \times 10^{10} M_\odot = 6.68 \times 10^{40}\,\mathrm{kg}$. Then

$$I = \sqrt{\frac{2\pi\,(1.80 \times 10^{10})\,(6.68 \times 10^{40})}{(4\pi \times 10^{-7})\,(3.086 \times 10^{19})}} = 1.4 \times 10^{19}\ \mathrm{A}.$$

Over all 175 galaxies, the fitted currents have median 4.3×10^{18} A, 16th–84th percentile 8.6×10^{17}–2.9×10^{19} A, and full range 3.8×10^{11}–1.4×10^{20} A (Figure 4, left). 15% of galaxies lie in 10^{17}–10^{18} A, and 83% lie above 10^{18} A, the current derived in the 3C 303 jet (Kronberg et al., 2011). The gas-only variant gives a median of 2.9×10^{18} A (16th–84th percentile 7.1×10^{17}–1.2×10^{19} A).

5.4 Implied magnetic field

The field implied by each fit follows from Eq. (2) with the fitted I and r_c, evaluated at $r = 10\,\mathrm{kpc}$:

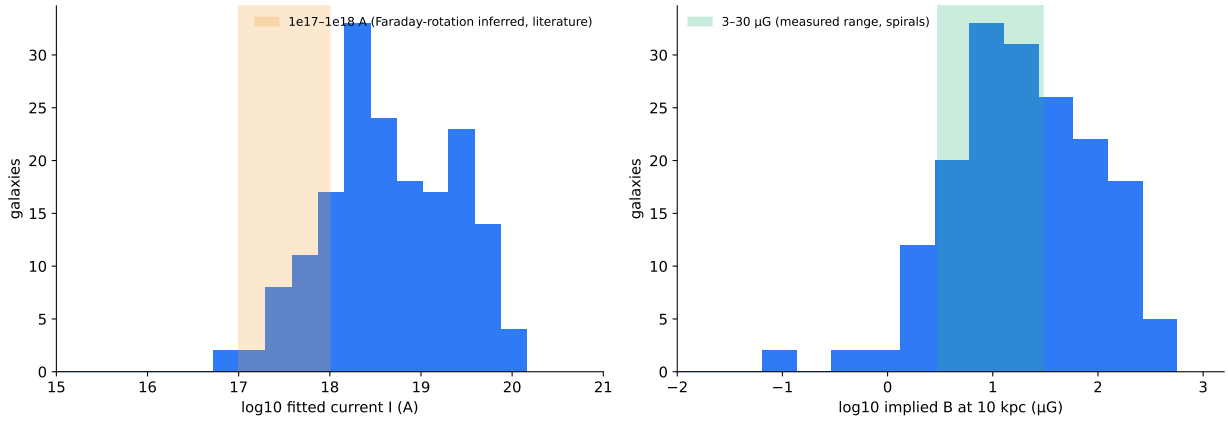


Figure 4: Left: fitted current I (Eq. 10, $L = 1\,\mathrm{kpc}$). The shaded band marks 10^{17}–$10^{18}\,\mathrm{A}$; the upper edge is the value derived for the 3C 303 jet. Right: implied field at 10 kpc. The shaded band marks the 3–30 μG range of fields measured in spiral galaxies.

1. Convert to SI: $r = 3.086 \times 10^{20}\,\mathrm{m}$, r_c (kpc) $\times\, 3.086 \times 10^{19}\,\mathrm{m}$.
2. Compute $B_{10} = \dfrac{\mu_0 I}{2\pi} \dfrac{r}{r^2 + r_c^2}$ in T.
3. Convert to microgauss: divide by $10^{-10}\,\mathrm{T}$.

For NGC 3198 ($I = 1.4 \times 10^{19}\,\mathrm{A}$, $r_c = 5.47\,\mathrm{kpc}$) this gives $B_{10} = 7.0 \times 10^{-9}\,\mathrm{T} = 70\,\mu\mathrm{G}$. Over the sample, B_{10} has median 15 μG, 16th–84th percentile 4.3–100 μG, and maximum 565 μG (Figure 4, right). For comparison with the measured values in Section 1: 11% of galaxies have $B_{10} < 3\,\mu\mathrm{G}$, 53% have $3 \le B_{10} \le 30\,\mu\mathrm{G}$, and 36% have $B_{10} > 30\,\mu\mathrm{G}$. 70% exceed the 74-galaxy average of 9 μG, and 49% exceed the 21-galaxy average of 17 μG (Beck, 2015). Because $B \propto I \propto L^{-1/2}$, these field values scale the same way as the currents with the assumed path length.

Inverse calculation from a measured field. One can instead take the field as given and ask what is required. Set $B_\phi(10\,\mathrm{kpc}) = 5\,\mu\mathrm{G}$. In the $r \gg r_c$ limit, the enclosed current is $I(< 10\,\mathrm{kpc}) = 2\pi r B/\mu_0 = 7.7 \times 10^{17}\,\mathrm{A}$. The fitted extra acceleration at 10 kpc, $a_{\mathrm{EM}} = Kr/(r^2 + r_c^2)$, has median $2.4 \times 10^{-11}\,\mathrm{m\,s^{-2}}$ (16th–84th percentile 0.9–6.3×10^{-11}). The required current-length per kilogram is then $\eta = a_{\mathrm{EM}}/B = 0.048\,\mathrm{A\,m\,kg^{-1}}$ (0.018–0.125). If the force is instead taken to act on a net charge q moving with the rotation ($F = qVB$), the required charge-to-mass ratio is $q/m = a_{\mathrm{EM}}/(VB) = 4.7 \times 10^{-7}\,\mathrm{C\,kg^{-1}}$ (2.9–7.2$\times 10^{-7}$). That equals 4.9×10^{-15} times the proton charge-to-mass ratio $e/m_p = 9.58 \times 10^{7}\,\mathrm{C\,kg^{-1}}$, or about five unbalanced elementary charges per 10^{15} protons.

5.5 Correlations with galaxy properties

Table 4 lists the correlations. The fitted core radius r_c correlates with the disk scale length with $\rho = 0.37$ ($p = 7 \times 10^{-7}$). Figure 5 plots $\sqrt{K}$ against V_{flat}.

6 Requirements and limitations, stated as quantities

R1. **Current magnitude.** With $L = 1\,\mathrm{kpc}$, 83% of galaxies require $I > 10^{18}\,\mathrm{A}$, the value derived for the 3C 303 jet. The median requirement is $4.3 \times 10^{18}\,\mathrm{A}$. Reaching the $10^{18}\,\mathrm{A}$ median would

Table 4: Spearman rank correlations between fitted E2 quantities and measured SPARC properties ($n = 175$, except $V_{\rm flat}$ with $n = 135$). All $p < 2 \times 10^{-14}$. The I column partly reflects the conversion itself, since $I \propto \sqrt{K M_b}$ (Eq. 10). The $\sqrt{K}$ column contains no mass input.

Property	$\rho(I)$	$\rho(\sqrt{K})$
Flat rotation velocity $V_{\rm flat}$	0.97	0.94
Baryonic mass M_b	0.91	0.72
3.6 μm luminosity	0.90	0.73
H I mass	0.83	0.63
Disk scale length R_d	0.72	0.54
Disk central surface brightness	0.62	0.56
Hubble type T	−0.81	−0.68

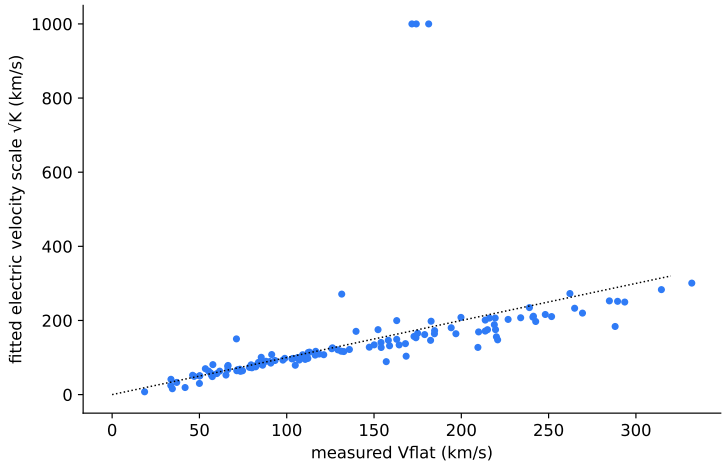


Figure 5: Fitted electromagnetic velocity scale $\sqrt{K}$ against the measured flat rotation velocity $V_{\rm flat}$, for the 135 galaxies with $V_{\rm flat}$ defined. The dotted line marks equality.

require $L \approx 19\,\mathrm{kpc}$ ($I \propto L^{-1/2}$).

R2. **Field strength.** 36% of galaxies imply $B_{10} > 30\,\mu$G, and 49% exceed the 17 μG bright-galaxy average. If instead B is fixed at a measured-like 5 μG, the matter must carry a current-length of about $0.05\,\mathrm{A\,m\,kg^{-1}}$, or a co-rotating net charge of about 5×10^{-15} of the proton charge per proton.

R3. **Coupling to neutral matter.** The rotation speeds are measured in mostly neutral H I and in stars. The model requires the electromagnetic force on the ionized component to be transferred to both (A5). No ion–neutral coupling rate or stellar coupling mechanism is computed here.

R4. **Free parameters.** K and r_c are fitted separately for each galaxy (350 parameters in total). They are not predicted from other measured properties. $\sqrt{K}$ correlates with $V_{\rm flat}$ ($\rho = 0.94$) and with M_b ($\rho = 0.72$), but no relation that would predict a rotation curve from photometry alone has been derived or tested.

R5. **Current closure and stability.** No return current, energy source, or time evolution of the current is modelled. The field energy implied by B_{10} and the stability of the configuration are

not checked.

R6. **Vertical and non-axisymmetric structure.** The model treats the disk as thin and axisymmetric. Measured galactic fields are mainly spiral and toroidal in the disk plane with X-shaped halo components (Beck, 2015), while Eq. (2) describes an azimuthal field from an axial current only. The geometries are not compared here.

R7. **Fitting systematics.** Distance and inclination uncertainties are not propagated (A9), and Υ is fixed in E2, BUR and NFW (a free-Υ_d variant is reported in Section 5.2). The $1\,\mathrm{km\,s^{-1}}$ error floor affects only points with smaller listed errors.

R8. **Sample size.** Larger public rotation-curve samples, such as PROBES (3,163 rotation curves; Stone et al. 2022) and MaNGA integral-field kinematics (Bundy et al., 2015), are a natural next test of the same models.

Cuddeford and Binney (1993) argued that a field strong enough to flatten a rotation curve would make the gas disk flare unacceptably, and Jokipii and Levy (1993) argued from the virial theorem that magnetic fields in an isolated galaxy are net expansive and cannot replace dark matter. Sánchez-Salcedo and Reyes-Ruiz (2004) concluded that azimuthal fields can contribute at most $\sim 10\,\mathrm{km\,s^{-1}}$ at the outermost H I point without a dark halo (up to $\sim 20\,\mathrm{km\,s^{-1}}$ with a halo); the present fits do not rebut those objections, and with $L = 1\,\mathrm{kpc}$ they require currents above $10^{18}\,\mathrm{A}$ in 83% of the galaxies and fields above $30\,\mu\mathrm{G}$ in 36%.

7 Testable predictions

Each item below follows from the fitted model and the assumptions in Section 3.6. Each one can be compared with independent radio measurements.

P1. **Field strength per galaxy.** Appendix A lists B_{10}, the predicted azimuthal field at 10 kpc, for every galaxy (with $L = 1\,\mathrm{kpc}$; $B \propto L^{-1/2}$). The largest predicted values are in UGC 2487 ($565\,\mu\mathrm{G}$), NGC 6674 ($301\,\mu\mathrm{G}$), NGC 5985 ($295\,\mu\mathrm{G}$), NGC 2841 ($279\,\mu\mathrm{G}$) and ESO 563-G021 ($270\,\mu\mathrm{G}$). Equipartition field estimates for these galaxies from synchrotron surveys would test the model directly.

P2. **Radial profile.** Eq. (2) predicts $B_\phi \propto r$ inside r_c and $B_\phi \propto 1/r$ outside, with the turnover at the fitted r_c (median 3.4 kpc). Resolved field-strength profiles from deep radio continuum maps can be compared with this shape.

P3. **Field geometry and sign.** An axial current produces an azimuthal field that circles the axis in one direction throughout the disk. In an inclined disk, the line-of-sight component of such a field follows the same pattern as the line-of-sight rotation velocity. Faraday-rotation maps would then show a rotation measure that is largest in magnitude near the major axis and reverses sign across the minor axis, with no large-scale reversals with radius. Reversals with radius in a given galaxy would conflict with a single axial current.

P4. **Current along the axis.** The model requires net axial currents of order 10^{18}–$10^{19}\,\mathrm{A}$. Rotation-measure gradients across disks and in the halos of edge-on galaxies, of the kind used for the 3C 303 jet (Kronberg et al., 2011), can measure or bound such currents.

P5. **Instruments.** Current LOFAR observations and future Square Kilometre Array surveys of polarized emission and background-source rotation measures (Beck, 2015) have the sensitivity and resolution intended for this kind of measurement in nearby disk galaxies.

8 Summary of measured results

- Newtonian baryons alone: median $\chi^2_\nu = 85$; 3% of galaxies with $\chi^2_\nu < 2$.
- $1/r$ filament (one parameter): median $\chi^2_\nu = 11.7$; 11% below 2.
- Bennett pinch with core (two parameters): median $\chi^2_\nu = 0.71$; 73% below 2. Same procedure, two parameters each: Burkert halo 0.71 and 70%; NFW halo 1.28 and 59%; RAR 1.35 and 64%.
- Head to head, the Bennett-pinch fit has the lower χ^2 in 117 of 175 galaxies against Burkert, 135 against NFW and 128 against RAR, and the lowest summed χ^2, AIC and BIC of the four. Published Burkert fits (Li et al., 2020): 0.97 and 69%.
- Required currents (with $L = 1\,\mathrm{kpc}$): median 4.3×10^{18} A; 83% above 10^{18} A.
- Implied fields at 10 kpc: median 15 μG; 53% within 3–30 μG; 36% above 30 μG.

Acknowledgments

This paper rests on the work of many people, and it is a pleasure to credit them specifically. Willard H. Bennett worked out in 1934 how a current stream confines itself with its own magnetic field; that equilibrium is the core of the model tested here. Hannes Alfvén described cosmic plasmas in terms of currents, circuits and double layers, and so opened the line of inquiry this paper follows. Anthony L. Peratt, with James C. Green, carried out the particle-in-cell simulations of interacting galactic-scale current filaments that motivated the $1/r$ and cored forms used here. Kristian Birkeland identified field-aligned currents in the polar atmosphere; the term Birkeland current used here follows that work. A. H. Nelson showed that magnetic stress in the outer gaseous disk can raise rotation speeds above the gravitational speed of the visible matter. E. Battaner, J. L. Garrido, M. Membrado and E. Florido developed an azimuthal-field account of flat rotation and a two-dimensional magnetohydrodynamic model of it. B. Ruiz-Granados, J. A. Rubiño-Martín, J. Calvo, E. Florido and E. Battaner fitted a magnetic contribution to the outer rotation curves of M31 and the Milky Way. D. Tsiklauri fitted a $\mathbf{J} \times \mathbf{B}$ term to the Milky Way rotation curve. Lee Holmes applied a magnetohydrodynamic boundary-stress analysis to the SPARC sample. Federico Lelli, Stacy S. McGaugh and James M. Schombert assembled SPARC and made its rotation curves and mass models freely available; without that careful, public data set this test could not have been done. Mordehai Milgrom proposed MOND, and McGaugh, Lelli and Schombert measured the radial acceleration relation whose fitting function serves as a reference curve here. Andreas Burkert introduced the cored halo profile, and Julio F. Navarro, Carlos S. Frenk and Simon D. M. White the NFW profile. Pengfei Li, Lelli, McGaugh and Schombert published the halo fits to SPARC used as a cross-check in Section 5.2. Philipp P. Kronberg, Richard V. E. Lovelace, Giovanni Lapenta and Stirling A. Colgate derived the current in the 3C 303 jet from Faraday rotation. Rainer Beck and the observers whose synchrotron and Faraday-rotation work he reviews measured the field strengths of spiral galaxies. Federica Govoni and the LOFAR team measured the radio ridge between Abell 399 and Abell 401. The author also thanks the many radio and optical observers whose original rotation curves are compiled in SPARC.

This work uses the SPARC database (Lelli et al., 2016). SPARC asks users of its data to cite the SPARC master paper, which we do, and to consider citing the original H I and Hα rotation-curve sources. Those sources are listed galaxy by galaxy in SPARC Table 1 (`SPARC_Lelli2016c.mrt`), which we used without modification. The author thanks Federico Lelli, Stacy S. McGaugh and James M. Schombert for assembling SPARC and making it public, and the many radio and optical observers whose original rotation curves are compiled there. We also used the machine-readable

halo-fit table of Li et al. (2020). The analysis uses NumPy (Harris et al., 2020), SciPy (Virtanen et al., 2020) and Matplotlib (Hunter, 2007). The paper was typeset with Tectonic (Williams, 2022).

Licenses

The text and figures of this paper are released under the Creative Commons Attribution 4.0 International license (CC BY 4.0). The analysis code in `anc/` is released under the MIT license. The SPARC data are not redistributed here and remain subject to the terms of their providers.

Data and code availability

The SPARC data (Lelli et al., 2016) are public at `https://astroweb.cwru.edu/SPARC/`. The Li et al. (2020) halo-fit table is the machine-readable Table 1 of that article. The analysis code (`fit.py`, `plots.py`), per-galaxy results (`results.csv`, `results.json`), aggregate statistics (`summary.json`) and model curves (`curves.json`) are included in the `anc/` directory of the source distribution of this paper, together with the same-procedure halo and RAR comparison (`compare.py`, `nfw_bounds_check.py`, `compare_results.csv`, `compare_summary.json`). Running `python fit.py`, `python plots.py` and `python compare.py` (Python 3, NumPy, SciPy 1.18, Matplotlib) on the SPARC files reproduces every number and figure.

Use of AI tools

An AI assistant (Grok Bot) helped write the analysis code and draft the text. The author directed the work, checked the results, and takes full responsibility for the content.

References

Hannes Alfvén. *Cosmic Plasma*, volume 82 of *Astrophysics and Space Science Library*. D. Reidel (Springer Netherlands), Dordrecht, 1981. doi: 10.1007/978-94-009-8374-8.

Hannes Alfvén. Double layers and circuits in astrophysics. *IEEE Transactions on Plasma Science*, 14(6):779–793, 1986. doi: 10.1109/TPS.1986.4316626.

E. Battaner and E. Florido. A two-dimensional model of magnetohydrodynamically driven rotation of spiral galaxies without dark matter. *Monthly Notices of the Royal Astronomical Society*, 277 (3):1129–1133, 1995. doi: 10.1093/mnras/277.3.1129.

E. Battaner, J. L. Garrido, M. Membrado, and E. Florido. Magnetic fields as an alternative explanation for the rotation curves of spiral galaxies. *Nature*, 360(6405):652–653, 1992. doi: 10.1038/360652a0.

Rainer Beck. Magnetic fields in spiral galaxies. *The Astronomy and Astrophysics Review*, 24:4, 2015. doi: 10.1007/s00159-015-0084-4.

Willard H. Bennett. Magnetically self-focussing streams. *Physical Review*, 45(12):890–897, 1934. doi: 10.1103/PhysRev.45.890.

Kristian Birkeland. *The Norwegian Aurora Polaris Expedition 1902–1903*, volume 1. H. Aschehoug & Co., Christiania, 1908.

A. Bosma. 21-cm line studies of spiral galaxies. II. the distribution and kinematics of neutral hydrogen in spiral galaxies of various morphological types. *The Astronomical Journal*, 86:1825–1846, 1981. doi: 10.1086/113063.

Kevin Bundy, Matthew A. Bershady, David R. Law, et al. Overview of the SDSS-IV MaNGA survey: Mapping nearby galaxies at Apache Point Observatory. *The Astrophysical Journal*, 798 (1):7, 2015. doi: 10.1088/0004-637X/798/1/7.

A. Burkert. The structure of dark matter halos in dwarf galaxies. *The Astrophysical Journal Letters*, 447:L25–L28, 1995. doi: 10.1086/309560.

P. Cuddeford and J. J. Binney. Galaxies and magnetic fields. *Nature*, 365(6441):20, 1993. doi: 10.1038/365020a0.

F. Govoni, E. Orrù, A. Bonafede, et al. A radio ridge connecting two galaxy clusters in a filament of the cosmic web. *Science*, 364(6444):981–984, 2019. doi: 10.1126/science.aat7500.

J. L. Han. Observing interstellar and intergalactic magnetic fields. *Annual Review of Astronomy and Astrophysics*, 55(1):111–157, 2017. doi: 10.1146/annurev-astro-091916-055221.

Charles R. Harris, K. Jarrod Millman, Stéfan J. van der Walt, et al. Array programming with NumPy. *Nature*, 585:357–362, 2020. doi: 10.1038/s41586-020-2649-2.

Lee Holmes. Magnetohydrodynamic boundary stress and galactic rotation curve anomalies. OSF Preprints, 2026. Preprint, posted 2026 January 1. doi: 10.17605/OSF.IO/M67EC.

John D. Hunter. Matplotlib: A 2D graphics environment. *Computing in Science & Engineering*, 9 (3):90–95, 2007. doi: 10.1109/MCSE.2007.55.

Ronnie Jansson and Glennys R. Farrar. A new model of the galactic magnetic field. *The Astrophysical Journal*, 757(1):14, 2012. doi: 10.1088/0004-637X/757/1/14.

J. R. Jokipii and E. H. Levy. Galaxies and magnetic fields. *Nature*, 365(6441):19–20, 1993. doi: 10.1038/365019b0.

Philipp P. Kronberg, Richard V. E. Lovelace, Giovanni Lapenta, and Stirling A. Colgate. Measurement of the electric current in a kpc-scale jet. *The Astrophysical Journal Letters*, 741(1):L15, 2011. doi: 10.1088/2041-8205/741/1/L15.

Federico Lelli, Stacy S. McGaugh, and James M. Schombert. SPARC: Mass models for 175 disk galaxies with Spitzer photometry at 3.6 μm and accurate rotation curves. *The Astronomical Journal*, 152(6):157, 2016. doi: 10.3847/0004-6256/152/6/157.

Federico Lelli, Stacy S. McGaugh, James M. Schombert, and Marcel S. Pawlowski. One law to rule them all: The radial acceleration relation of galaxies. *The Astrophysical Journal*, 836(2): 152, 2017. doi: 10.3847/1538-4357/836/2/152.

Pengfei Li, Federico Lelli, Stacy McGaugh, and James Schombert. A comprehensive catalog of dark matter halo models for SPARC galaxies. *The Astrophysical Journal Supplement Series*, 247(1): 31, 2020. doi: 10.3847/1538-4365/ab700e.

Stacy S. McGaugh, Federico Lelli, and James M. Schombert. Radial acceleration relation in rotationally supported galaxies. *Physical Review Letters*, 117(20):201101, 2016. doi: 10.1103/PhysRevLett.117.201101.

M. Milgrom. A modification of the Newtonian dynamics as a possible alternative to the hidden mass hypothesis. *The Astrophysical Journal*, 270:365–370, 1983. doi: 10.1086/161130.

Julio F. Navarro, Carlos S. Frenk, and Simon D. M. White. The structure of cold dark matter halos. *The Astrophysical Journal*, 462:563–575, 1996. doi: 10.1086/177173.

A. H. Nelson. On the influence of galaxy magnetic fields on the rotation curves in the outer discs of galaxies. *Monthly Notices of the Royal Astronomical Society*, 233(1):115–121, 1988. doi: 10.1093/mnras/233.1.115.

Anthony L. Peratt. Evolution of the plasma universe: I. double radio galaxies, quasars, and extragalactic jets. *IEEE Transactions on Plasma Science*, 14(6):639–660, 1986a. doi: 10.1109/TPS.1986.4316615.

Anthony L. Peratt. Evolution of the plasma universe: II. the formation of systems of galaxies. *IEEE Transactions on Plasma Science*, 14(6):763–778, 1986b. doi: 10.1109/TPS.1986.4316625.

Anthony L. Peratt and James C. Green. On the evolution of interacting, magnetized, galactic plasmas. *Astrophysics and Space Science*, 91(1):19–33, 1983. doi: 10.1007/BF00650210.

Vera C. Rubin, Jr. Ford, W. Kent, and Norbert Thonnard. Rotational properties of 21 Sc galaxies with a large range of luminosities and radii, from NGC 4605 (R = 4 kpc) to UGC 2885 (R = 122 kpc). *The Astrophysical Journal*, 238:471–487, 1980. doi: 10.1086/158003.

B. Ruiz-Granados, J. A. Rubiño-Martín, E. Florido, and E. Battaner. Magnetic fields and the outer rotation curve of M31. *The Astrophysical Journal Letters*, 723(1):L44–L48, 2010. doi: 10.1088/2041-8205/723/1/L44.

B. Ruiz-Granados, E. Battaner, J. Calvo, E. Florido, and J. A. Rubiño-Martín. Dark matter, magnetic fields, and the rotation curve of the Milky Way. *The Astrophysical Journal Letters*, 755 (2):L23, 2012. doi: 10.1088/2041-8205/755/2/L23.

F. J. Sánchez-Salcedo and M. Reyes-Ruiz. Constraining the magnetic effects on H I rotation curves and the need for dark halos. *The Astrophysical Journal*, 607(1):247–257, 2004. doi: 10.1086/383229.

James Schombert and Stacy McGaugh. Stellar populations and the star formation histories of LSB galaxies: III. stellar population models. *Publications of the Astronomical Society of Australia*, 31:e036, 2014. doi: 10.1017/pasa.2014.32.

Yoshiaki Sofue and Vera Rubin. Rotation curves of spiral galaxies. *Annual Review of Astronomy and Astrophysics*, 39(1):137–174, 2001. doi: 10.1146/annurev.astro.39.1.137.

Connor Stone, Stéphane Courteau, Nikhil Arora, Matthew Frosst, and Thomas H. Jarrett. PROBES. I. a compendium of deep rotation curves and matched multiband photometry. *The Astrophysical Journal Supplement Series*, 262(1):33, 2022. doi: 10.3847/1538-4365/ac83ad.

D. Tsiklauri. Galaxy rotation curves: the effect of $\vec{j} \times \vec{B}$ force. *Astrophysics and Space Science*, 334:165–170, 2011. doi: 10.1007/s10509-011-0703-0.

Pauli Virtanen, Ralf Gommers, Travis E. Oliphant, et al. SciPy 1.0: Fundamental algorithms for scientific computing in Python. *Nature Methods*, 17:261–272, 2020. doi: 10.1038/s41592-019-0686-2.

Peter K. G. Williams. The Tectonic project: Envisioning a 21st-century TeX experience. *TUGboat*, 43(2):120–126, 2022. doi: 10.47397/tb/43-2/tb134williams-tectonic.

A Per-galaxy results

Table 5: Per-galaxy fit results for all 175 SPARC galaxies. N = number of rotation-curve points; Q = SPARC quality flag; columns N, E1, E2, R0, R2 give χ^2_ν for each model (Section 3); I = current from Eq. (10) with $L = 1\,\mathrm{kpc}$ (A); r_c = fitted core radius (kpc); B_{10} = implied field at 10 kpc (μG). A galaxy with E2 χ^2_ν near 1 is fitted to within its errors. Compare B_{10} with the 3–30 μG measured range.

Galaxy	N	Q	N	E1	E2	R0	R2	I (A)	r_c	B_{10}
CamB	9	2	5.00	5.63	4.50	108	4.81	4.2×10^{18}	170	0.09
D512-2	4	2	23.6	2.75	0.07	2.66	0.12	3.4×10^{17}	1.44	2.15
D564-8	6	2	39.4	11.6	0.04	18.3	0.99	1.2×10^{17}	2.01	0.74
D631-7	16	1	106	46.2	0.88	30.1	10.6	1.0×10^{18}	6.59	4.56
DDO064	14	1	12.9	5.22	0.34	0.40	0.31	5.6×10^{17}	1.80	3.52
DDO154	12	2	532	77.9	0.71	16.0	0.40	5.5×10^{17}	2.47	3.38
DDO161	31	1	329	37.6	0.27	138	0.91	1.8×10^{18}	7.13	7.61
DDO168	10	2	161	47.3	3.94	30.1	15.8	1.0×10^{18}	3.48	5.83
DDO170	8	2	599	23.8	1.29	152	2.95	1.1×10^{18}	3.81	6.44
ESO079-G014	15	1	395	54.7	0.91	7.99	3.47	1.6×10^{19}	7.68	66.4
ESO116-G012	15	1	330	70.7	0.88	12.9	2.06	3.7×10^{18}	3.44	21.2
ESO444-G084	7	2	285	62.7	1.92	27.8	1.47	5.3×10^{17}	1.40	3.37
ESO563-G021	30	1	246	98.1	9.04	53.5	17.2	7.0×10^{19}	8.21	270
F561-1	6	3	3.65	0.48	0.41	40.2	0.83	1.1×10^{18}	1.73	6.97
F563-1	17	1	31.7	7.49	0.48	2.78	1.09	4.3×10^{18}	3.64	24.7
F563-V1	6	3	0.98	0.31	0.22	34.4	0.32	3.6×10^{17}	1.73	2.30
F563-V2	10	1	22.7	12.0	0.18	4.33	0.40	4.4×10^{18}	2.62	26.6
F565-V2	7	2	43.3	5.71	0.04	1.09	0.32	1.8×10^{18}	5.07	9.06
F567-2	5	3	12.9	1.03	0.44	5.64	0.36	1.7×10^{18}	2.40	10.3
F568-1	12	1	40.1	12.6	0.07	6.90	0.83	7.1×10^{18}	3.69	40.4
F568-3	18	1	29.5	16.1	0.89	2.78	2.86	5.7×10^{18}	6.22	26.6
F568-V1	15	1	45.6	1.88	0.08	9.40	0.31	4.7×10^{18}	2.69	28.2
F571-8	13	1	165	91.2	10.3	40.6	20.5	8.4×10^{18}	9.20	29.4
F571-V1	7	2	39.9	3.57	0.03	0.78	0.21	2.4×10^{18}	5.15	12.1
F574-1	14	1	113	24.6	0.10	3.52	1.51	4.7×10^{18}	3.26	27.6
F574-2	5	3	0.09	0.05	0.04	22.1	0.05	4.6×10^{17}	3.76	2.63
F579-V1	14	1	28.0	3.00	0.01	3.49	1.52	5.2×10^{18}	1.12	33.5
F583-1	25	1	50.6	12.0	0.19	3.65	1.58	2.7×10^{18}	4.28	15.0
F583-4	12	1	38.2	9.88	0.41	1.31	0.12	1.4×10^{18}	2.14	8.63
IC2574	34	2	184	55.3	1.51	73.1	0.71	1.9×10^{18}	9.47	6.63
IC4202	32	1	151	96.8	31.9	37.4	34.8	3.6×10^{19}	6.95	160
KK98-251	15	2	21.4	11.7	0.27	29.4	0.67	3.3×10^{17}	3.00	1.95
NGC0024	29	1	89.4	12.4	0.30	10.5	0.66	3.0×10^{18}	1.17	19.4
NGC0055	21	2	101	27.7	0.38	44.8	0.60	3.2×10^{18}	6.47	14.5
NGC0100	21	1	51.5	15.9	0.07	1.87	0.33	3.3×10^{18}	4.47	18.0
NGC0247	26	2	284	49.6	3.28	3.77	1.68	3.5×10^{18}	2.75	21.0
NGC0289	28	2	149	2.90	2.03	11.6	1.86	2.3×10^{19}	6.16	107
NGC0300	25	2	161	22.6	0.55	2.41	0.80	2.7×10^{18}	3.49	15.7
NGC0801	13	1	195	27.4	7.39	86.9	5.63	3.8×10^{19}	3.13	226
NGC0891	18	1	164	41.7	14.1	34.2	4.30	3.2×10^{19}	14.5	67.3
NGC1003	36	1	592	26.1	4.76	13.1	4.69	6.4×10^{18}	7.85	25.5

Galaxy	N	Q	N	E1	E2	R0	R2	I (A)	r_c	B_{10}
NGC1090	24	1	377	27.8	1.37	44.2	2.51	1.7×10^{19}	5.62	81.9
NGC1705	14	3	96.0	0.85	0.14	14.5	0.09	8.1×10^{17}	0.31	5.26
NGC2366	26	3	89.8	33.1	0.82	25.4	1.53	9.0×10^{17}	2.50	5.49
NGC2403	73	1	927	223	17.0	16.7	6.22	6.4×10^{18}	3.09	37.9
NGC2683	11	2	62.7	1.52	1.06	2.14	1.08	1.6×10^{19}	2.58	99.5
NGC2841	50	1	746	3.77	1.49	86.3	2.24	4.7×10^{19}	3.01	279
NGC2903	34	1	736	55.8	10.1	12.6	7.75	2.0×10^{19}	6.34	90.7
NGC2915	30	2	59.0	3.52	0.56	7.61	1.66	1.5×10^{18}	1.84	9.28
NGC2955	24	1	17.0	8.18	4.55	7.96	3.90	5.0×10^{19}	13.6	113
NGC2976	27	2	16.6	9.50	0.29	3.04	0.68	2.5×10^{18}	2.77	15.0
NGC2998	13	1	584	6.08	3.18	15.5	2.65	3.1×10^{19}	1.60	198
NGC3109	25	1	145	78.8	0.16	4.96	2.24	1.2×10^{18}	4.21	6.44
NGC3198	43	1	738	39.5	0.77	13.3	2.25	1.4×10^{19}	5.47	69.6
NGC3521	41	1	15.2	3.88	0.82	0.76	0.51	2.1×10^{19}	5.16	109
NGC3726	12	2	48.1	9.40	2.37	25.0	2.75	1.6×10^{19}	11.5	45.6
NGC3741	21	1	123	22.3	1.34	1.35	0.23	4.6×10^{17}	2.51	2.80
NGC3769	12	2	53.8	4.79	0.57	4.65	0.82	8.0×10^{18}	5.63	39.5
NGC3877	13	2	31.8	9.42	4.37	13.1	7.93	1.2×10^{19}	2.41	70.5
NGC3893	10	1	49.7	7.50	0.37	0.90	0.64	1.7×10^{19}	4.76	88.5
NGC3917	17	1	158	40.7	0.99	2.86	2.67	8.0×10^{18}	4.48	43.3
NGC3949	7	2	6.83	2.07	0.44	2.26	0.38	1.7×10^{19}	10.0	56.3
NGC3953	8	1	61.4	1.17	0.20	2.48	0.58	2.3×10^{19}	2.87	137
NGC3972	10	1	85.7	20.4	0.75	1.90	1.36	6.2×10^{18}	3.58	35.5
NGC3992	9	1	287	0.69	0.48	9.24	1.07	4.4×10^{19}	3.58	251
NGC4010	12	2	56.3	17.2	1.42	3.99	1.62	7.8×10^{18}	6.65	35.1
NGC4013	36	2	153	8.03	1.67	7.48	1.67	1.9×10^{19}	9.86	61.1
NGC4051	7	2	11.2	1.11	0.68	11.4	1.49	1.1×10^{19}	2.77	68.8
NGC4068	6	2	16.1	8.30	0.21	24.5	0.24	1.8×10^{18}	12.0	4.68
NGC4085	7	2	14.2	12.3	4.53	13.1	3.16	1.7×10^{19}	17.6	27.5
NGC4088	12	1	12.4	6.82	1.00	35.9	0.64	1.4×10^{20}	175	3.05
NGC4100	24	1	140	2.40	0.95	3.39	1.39	1.5×10^{19}	2.92	91.4
NGC4138	7	2	21.9	1.12	1.01	1.21	1.12	1.1×10^{19}	2.07	70.0
NGC4157	17	1	39.8	6.32	0.39	9.09	0.66	2.5×10^{19}	15.4	47.8
NGC4183	23	1	75.8	3.69	0.16	3.69	0.40	5.4×10^{18}	2.65	32.8
NGC4214	14	2	46.9	2.15	1.45	5.67	0.97	1.4×10^{18}	0.67	9.25
NGC4217	19	1	43.1	45.0	33.7	55.7	34.6	1.2×10^{20}	122	5.29
NGC4389	6	3	14.0	16.8	21.0	54.0	3.58	3.8×10^{11}	55.8	0.00
NGC4559	32	1	78.4	6.41	0.29	13.9	0.52	8.1×10^{18}	6.59	36.4
NGC5005	18	1	2.26	1.93	0.42	0.54	0.44	4.7×10^{19}	14.0	102
NGC5033	22	1	950	14.3	5.63	13.9	8.87	2.7×10^{19}	5.55	135
NGC5055	28	1	724	250	10.4	322	3.21	2.8×10^{19}	15.2	54.8
NGC5371	19	1	134	4.71	4.98	171	10.5	3.1×10^{19}	0.01	202
NGC5585	24	1	285	174	5.26	25.8	6.25	3.1×10^{18}	4.24	16.9
NGC5907	19	1	1066	3.81	3.74	33.6	6.38	3.4×10^{19}	2.35	208
NGC5985	33	1	755	5.11	1.90	161	19.7	4.9×10^{19}	2.77	295
NGC6015	44	2	457	61.6	7.12	33.7	10.4	1.1×10^{19}	1.96	69.5
NGC6195	23	1	29.8	13.4	2.18	26.6	1.83	5.6×10^{19}	25.3	49.6
NGC6503	31	1	1664	21.0	1.37	2.81	2.67	5.7×10^{18}	3.58	32.5
NGC6674	15	1	2259	6.18	6.65	24.5	9.07	4.7×10^{19}	0.01	301
NGC6789	4	2	21.8	11.1	0.29	6.11	1.14	4.9×10^{17}	1.08	3.15
NGC6946	58	1	161	22.7	1.75	25.6	2.09	1.5×10^{19}	6.04	71.6
NGC7331	36	1	242	38.1	3.97	35.8	1.17	5.0×10^{19}	23.8	48.5
NGC7793	46	1	14.8	6.80	1.04	0.91	0.77	3.2×10^{18}	1.73	20.0
NGC7814	18	1	405	10.9	0.69	27.3	1.19	2.1×10^{19}	5.53	105
PGC51017	6	3	1.56	1.07	1.33	131	2.14	8.0×10^{16}	0.01	0.52
UGC00128	22	1	3386	25.9	2.77	74.4	5.15	8.6×10^{18}	6.18	40.5
UGC00191	9	1	568	123	1.59	18.7	2.54	2.2×10^{18}	1.76	13.6

Galaxy	N	Q	N	E1	E2	R0	R2	I (A)	r_c	B_{10}
UGC00634	4	2	1456	28.6	0.64	1.40	1.19	4.9×10^{18}	6.56	22.2
UGC00731	12	1	195	17.8	0.37	16.4	7.56	1.9×10^{18}	2.03	11.7
UGC00891	5	2	754	63.1	0.15	24.8	7.51	1.1×10^{18}	5.01	5.77
UGC01230	11	1	22.8	5.15	0.48	3.69	0.98	6.2×10^{18}	3.18	36.3
UGC01281	25	1	24.4	12.6	0.14	0.37	0.20	8.6×10^{17}	3.09	5.08
UGC02023	5	2	2.99	2.00	0.06	2.56	0.27	2.0×10^{19}	80.9	1.99
UGC02259	8	2	670	8.55	0.76	45.6	3.45	1.8×10^{18}	1.22	11.2
UGC02455	8	3	23.5	26.9	31.4	125	1.58	1.4×10^{13}	40.6	0.00
UGC02487	17	1	2849	9.32	9.94	262	3.31	8.9×10^{19}	1.28	565
UGC02885	19	1	132	7.27	4.00	2.83	2.82	7.2×10^{19}	13.0	174
UGC02916	43	2	103	77.6	33.0	72.2	38.0	3.4×10^{19}	13.4	79.7
UGC02953	115	2	1788	55.4	3.73	144	4.95	4.9×10^{19}	4.92	258
UGC03205	48	1	550	7.70	2.65	12.3	6.18	2.6×10^{19}	2.41	161
UGC03546	30	1	660	13.7	2.27	9.05	2.54	2.2×10^{19}	7.64	88.8
UGC03580	47	2	415	152	20.5	86.4	29.3	8.0×10^{18}	10.4	24.8
UGC04278	25	1	57.3	17.3	0.71	3.20	2.48	2.8×10^{18}	5.79	13.8
UGC04305	22	3	2.88	2.31	1.84	68.5	1.86	3.2×10^{17}	0.70	2.08
UGC04325	8	1	229	21.2	0.65	29.3	5.47	2.1×10^{18}	1.24	13.5
UGC04483	8	2	30.0	6.10	0.24	11.3	0.46	8.7×10^{16}	0.51	0.57
UGC04499	9	1	108	13.8	0.22	9.48	1.28	1.8×10^{18}	2.83	10.8
UGC05005	11	1	15.1	6.50	0.02	2.46	0.16	4.4×10^{18}	10.0	14.1
UGC05253	73	2	352	85.0	2.42	6.89	5.10	3.7×10^{19}	8.09	147
UGC05414	6	1	63.4	20.5	0.12	11.1	0.08	1.3×10^{18}	2.96	7.68
UGC05716	12	2	1217	33.0	2.32	22.8	3.71	1.6×10^{18}	2.80	9.79
UGC05721	23	1	85.2	11.2	0.58	12.3	1.62	1.4×10^{18}	0.84	8.89
UGC05750	11	1	14.3	8.99	0.11	3.21	0.53	2.4×10^{18}	7.02	10.6
UGC05764	10	2	666	36.6	2.27	59.2	9.52	4.9×10^{17}	0.94	3.14
UGC05829	11	2	23.9	5.24	0.24	2.86	0.06	1.3×10^{18}	2.99	7.88
UGC05918	8	2	30.8	3.69	0.03	1.21	0.26	5.2×10^{17}	1.35	3.32
UGC05986	15	2	354	72.4	0.93	30.1	2.78	5.0×10^{18}	3.16	29.4
UGC05999	5	2	78.5	13.8	0.87	5.80	3.66	3.7×10^{18}	7.39	15.4
UGC06399	9	1	71.8	9.78	0.04	0.77	0.38	2.2×10^{18}	3.31	12.8
UGC06446	17	1	97.3	4.40	0.29	4.88	0.23	2.1×10^{18}	1.59	13.0
UGC06614	13	1	27.2	8.67	0.20	9.17	2.87	3.6×10^{19}	26.3	29.3
UGC06628	7	2	0.66	0.28	0.34	16.3	0.51	6.7×10^{17}	0.01	4.36
UGC06667	9	1	224	26.2	0.13	26.7	3.46	2.1×10^{18}	2.92	12.4
UGC06786	45	1	1306	50.3	1.86	170	1.35	2.4×10^{19}	4.93	127
UGC06787	71	2	1314	89.5	23.4	169	25.6	2.9×10^{19}	6.11	137
UGC06818	8	2	25.1	11.9	1.17	8.37	1.18	4.0×10^{18}	13.1	9.60
UGC06917	11	1	129	12.6	0.17	1.44	1.13	4.4×10^{18}	3.45	25.5
UGC06923	6	2	30.6	5.21	0.45	2.21	0.82	2.3×10^{18}	3.24	13.4
UGC06930	10	1	57.4	2.93	0.09	2.53	0.46	5.0×10^{18}	3.14	29.3
UGC06973	9	3	73.0	82.1	83.5	91.0	1.68	9.7×10^{19}	81.0	9.45
UGC06983	17	1	113	4.02	0.38	3.62	0.89	4.6×10^{18}	2.79	27.8
UGC07089	12	2	22.1	7.13	0.18	10.0	0.16	2.6×10^{18}	5.94	12.2
UGC07125	13	1	80.9	7.60	0.31	142	1.40	2.6×10^{18}	4.36	14.1
UGC07151	11	1	117	23.4	0.79	3.85	1.77	1.6×10^{18}	1.46	10.0
UGC07232	4	2	18.2	8.43	0.11	1.62	0.45	6.2×10^{18}	21.5	7.10
UGC07261	7	2	34.1	1.80	0.20	0.66	0.55	1.9×10^{18}	1.21	12.2
UGC07323	10	1	37.0	13.4	0.33	5.71	0.26	2.7×10^{18}	4.57	14.5
UGC07399	10	1	329	27.6	0.46	76.4	1.49	2.2×10^{18}	1.35	13.8
UGC07524	31	1	103	21.5	0.29	5.29	1.28	2.5×10^{18}	3.38	14.4
UGC07559	7	2	9.24	3.65	0.09	10.5	0.33	3.2×10^{17}	1.88	1.97
UGC07577	9	2	0.59	0.39	0.13	17.1	0.32	5.1×10^{18}	157	0.13
UGC07603	12	1	118	20.7	0.18	5.63	0.85	8.3×10^{17}	1.45	5.25
UGC07608	8	1	25.0	6.03	0.07	1.31	0.42	1.2×10^{18}	2.77	7.27
UGC07690	7	2	27.9	1.14	0.26	2.05	0.40	8.5×10^{17}	0.59	5.48

Galaxy	N	Q	N	E1	E2	R0	R2	I (A)	r_c	B_{10}
UGC07866	7	2	7.41	1.47	0.07	3.94	0.04	2.3×10^{17}	0.93	1.49
UGC08286	17	1	468	28.5	0.58	27.2	1.95	1.7×10^{18}	1.50	10.8
UGC08490	30	1	148	5.94	0.22	5.80	0.25	1.6×10^{18}	0.96	10.3
UGC08550	11	1	201	16.6	0.57	2.57	1.20	6.8×10^{17}	1.10	4.38
UGC08699	41	2	159	12.1	1.63	6.44	0.87	1.4×10^{19}	2.78	86.8
UGC08837	8	2	17.8	13.3	0.35	36.8	0.90	6.5×10^{18}	45.5	1.93
UGC09037	22	2	34.1	20.7	4.11	45.6	1.63	2.4×10^{19}	23.4	24.4
UGC09133	68	1	1544	55.8	5.74	59.0	10.1	5.0×10^{19}	8.14	194
UGC09992	5	2	3.92	0.01	0.01	7.32	0.03	3.4×10^{17}	0.26	2.20
UGC10310	7	1	38.2	4.40	0.13	2.48	0.12	1.8×10^{18}	1.98	11.3
UGC11455	36	1	78.8	56.4	3.05	6.79	4.75	5.7×10^{19}	12.7	140
UGC11557	12	2	2.18	2.38	1.07	20.5	1.06	7.8×10^{18}	25.9	6.53
UGC11820	10	1	671	66.1	6.71	61.7	1.05	2.4×10^{18}	5.54	12.1
UGC11914	65	1	206	8.95	4.62	69.8	1.70	2.9×10^{19}	0.88	185
UGC12506	31	2	77.9	1.19	0.37	7.91	0.98	4.0×10^{19}	2.53	245
UGC12632	15	1	122	6.66	0.06	7.09	0.41	2.0×10^{18}	2.57	12.4
UGC12732	16	1	163	15.0	0.99	3.87	0.13	3.5×10^{18}	3.19	20.5
UGCA281	7	3	40.0	10.1	0.12	3.35	0.24	2.1×10^{17}	0.53	1.39
UGCA442	8	1	290	64.9	0.77	3.83	3.99	6.8×10^{17}	2.69	4.10
UGCA444	36	2	12.6	3.63	0.24	2.01	0.15	1.8×10^{17}	1.14	1.16